JOURNAL OF THERMOPHYSICS AND HEAT TRANSFER
Vol. 21, No. 1, January–March 2007

Shock-Tube Determination of CN Formation Rate in a CO–N_2 Mixture

Eun-Seok Lee,* Chul Park,† and Keun-Shik Chang‡
Korea Advanced Institute of Science and Technology, Daejeon 305-701, Republic of Korea

DOI: 10.2514/1.25144

The chemical process of CN formation in a CO–N_2 mixture is studied through temporally resolved intensity measurement of CN violet radiation occurring in the reflected-shock region of a shock tube. A 78% CO–22% N_2 mixture is driven by cold hydrogen to a shock speed of up to 3.45 km/s, to produce a reflected-shock temperature corresponding to Martian entry flight of up to 6.4 km/s. Absolute calibration of spectrometer is performed using a standard lamp of radiance. A reaction model is constructed by combining four existing models and multiplying the C_2 dissociation rate by a factor of five.

Nomenclature

k_f = forward reaction rate coefficient, $cm^3\ mole^{-1}\ s^{-1}$
M = unspecified third body
P = pressure, torr or atm
P_{1eq} = equivalent initial pressure for a reflected shock, torr
T = heavy-particle translational-rotational temperature, K
T_a = geometric average temperature, $\sqrt{TT_v}$, K
T_d = characteristic temperature of reaction, K
T_v = vibrational-electron-electronic temperature, K
T_x = unspecified temperature (T, T_a, or T_v), K
U_{eq} = equivalent shock velocity for a reflected shock, km/s
U_s = shock velocity in a shock tube, km/s
v = vibrational energy level of a molecule

Subscripts

1 = condition ahead of a shock wave
2 = condition immediately behind a shock wave
5 = condition in reflected-shock region

I. Introduction

We attempt to simulate the flow around a space vehicle entering the atmosphere of the planet Mars using a shock tube. In [1], a Mars entry mission was proposed as a future space mission of the Republic of Korea. We would like to determine the aerothermodynamic environment during the entry flight. The entry velocity of a typical Mars entry vehicle ranges from 5 to 9 km/s [2]. It flies through the atmosphere of Mars, which consists of 95.7% CO_2–2.7% N_2– 1.6% Ar by volume [3]. At the entry velocity of 6.5 km/s, the translational temperature immediately behind the standing shock wave reaches up to 30,000 K. CO_2 dissociates quickly, and the translational temperature falls and equilibrates with the vibrational temperature at some distance from the shock. The equilibrium temperature is about 6300 K.

The nonequilibrium thermochemical behavior of the CO_2–N_2 mixture has been studied by many researchers using a shock tube: Arnold et al. [4], Thomas and Menard [5], Nealy and Haggard [6,7], and Arnold and Nicholls [8]. But their experimental data show a substantial scatter and inconsistencies both in the equilibrium and nonequilibrium regions [2]. Some of these inconsistencies may be attributed to the use of an arc-heated driver [5–7]: Bogdanoff and Park [9] reported that the radiation from the arc-heated driver travels far downstream of the driven tube and disturbs the flow. More recently, extensive studies have been carried out by Russian researchers such as Zalogin [10], Losev [11], and Gorelov [12]. Zalogin and Losev made shock-tube measurements of CN and C_2 radiation using a CO–N_2 mixture diluted 1:10 or 1:20 by Argon to increase the temperature. In their work, the temporal dynamics of the radiation intensity was qualitatively studied. Gorelov also qualitatively measured nonequilibrium CN radiation by shock-heating a CO_2–air mixture and compared the measurement with the calculation.

Thus, the nonequilibrium flow condition in the shock layer during the entry flight into Mars is still uncertain. Because CO_2 dissociates quickly into CO and O, and because the chemical reactions between O and N_2 are relatively well known, the uncertainty in the Martian mixture exists mostly in the processes for CO–N_2 mixture. The goal of the present work is to study the thermochemical nonequilibrium process in the CO–N_2 mixture. The absolute emission of the CN violet band from a CO–N_2 mixture behind the reflected shock wave is measured in a shock tube using a spectrometer. The spectrometer is calibrated against a standard lamp of radiance. The measured intensity is compared with numerical calculations using the reaction rate models presented in four sources. A reaction model that combines these four models with the C_2 dissociation rate multiplied by a factor of five is seen to agree closest with the experimental data.

II. Shock-Tube Measurement

A. Shock-Tube and Test Conditions

In the shock tube used in the present work, the stainless steel driver with an internal diameter of 68 mm is designed to withstand the operating pressure of 100 atm. The driver temperature is the room temperature. The 3-m-long driven section is made of an aluminum alloy and has an internal diameter of 4.75 cm. A transition section is placed between the driver and the driven tube. The diaphragm made of polyethylene is mounted on the driver side. Two 3-mm-thick sapphire windows are installed on the front and back sides of the test section near the end wall. Both windows have an aperture of 25 mm in diameter. The center of the windows of the test section is 3.3 m from the diaphragm.

The present experiment is conducted under the following configurations: The driver gas is pure H_2 supplied from a 120-atm bottle. The diaphragm is ruptured in a passive manner: A 0.35-mm-thick polyethylene film ruptures at the driver fill pressure of 17 atm. Two such films are used to rupture at 34 atm. The rupture pressure is reproduced within 0.5 atm. A 78% CO–22% N_2 mixture is used as the test gas. This moderate mixture ratio is chosen to reduce the

---

Received 17 May 2006; revision received 23 June 2006; accepted for publication 23 June 2006.

*Graduate Student, Department of Aerospace Engineering; branden67@kaist.ac.kr.

†Professor, Department of Aerospace Engineering. Fellow AIAA.

‡Professor, Department of Aerospace Engineering. Member AIAA.

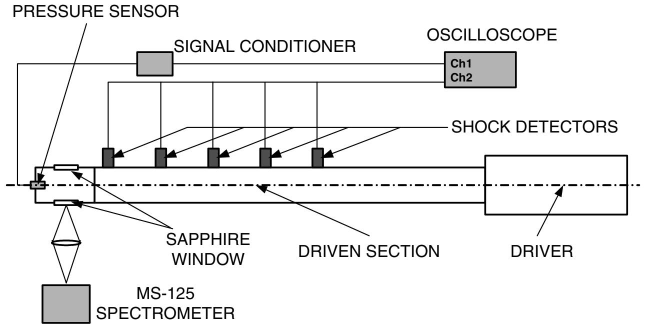

Fig. 1 Schematic of the instrumentations for flow measurement.

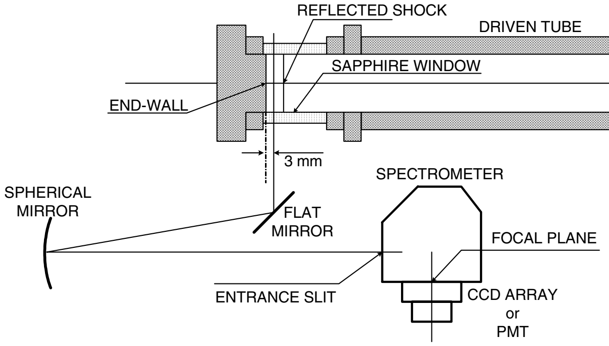

Fig. 2 Spectrometer setup.

uncertainty originating from the adsorption of gas molecules onto the inner wall of the shock tube. The test gas is premixed in an aluminum chamber by charging the two gases at the desired partial pressures. The mixture is allowed two days before use. The driven tube fill pressure is either 1.3 or 2.6 torr. The 1.3 and 2.6 torr cases produced shock velocities of 3.45 and 3.2 km/s, respectively, with the driver fill pressure of 17 atm. The other test condition of 2.6 torr–34 atm produced a shock velocity of 3.4 km/s, and postshock pressure increased by a factor of about two.

B. Instruments for Flow Measurement

Figure 1 describes the experimental setup. Uniformly separated five ionization gauges are placed along the driven tube to measure the speed of the primary shock. The shock wave, due to its high temperature behind it, ionizes the test gas, and the gauges are sequentially activated. The uncertainty in the measured shock-arrival time is within 1%. We calculate the shock speed from the time intervals between the activation events. A PCB model 111A21 quartz crystal pressure transducer is installed in the end wall of the shock tube to measure the pressure behind the reflected shock. The sensitivity of the transducer is 5 mV/psi.

An ORIEL MS125 spectrometer is used for the emission measurement. Gratings of 600 and 400 lines/mm are used for spectral and temporal measurements, respectively. The 600 lines/mm grating has a spectral resolution of 1.8 nm with a 50 μm entrance slit. The f-number of the internal optics (a collimator and a focusing mirror) of the spectrometer is 3.7. A flat mirror and a spherical mirror are used to transmit the light into the entrance slit. This external optical arrangement produced a 1:1 image of the light source with an f-number of 130.

Two types of detectors are used to record the spectrum imaged on the exit focal plane of the spectrometer. A 2048-element array of 14 μm-pixel CCDs is used as the detector for the spectral measurement. Being installed on the exit focal plane of the MS125 instrument, each element of the CCD array counts the photons delivered through the light ray dispersed by the grating in electric volts, yielding spectral intensity distribution. The CCD array integrates radiation over an 8-ms interval. The obtained spectral intensity signal is recorded by a 300 MHz digital oscilloscope.

For the temporal measurement, a variable-width slit assembly was placed on the exit focal plane of the spectrometer. We placed a Hamamatsu R7400U-03 photomultiplier tube (PMT) behind the slit. The signal produced by the PMT is recorded by the oscilloscope. The PCB pressure transducer triggers the oscilloscope at the instant the primary shock arrives at the end wall. The spectral response of the PMT ranges from 185 to 650 nm and its peak sensitivity is at 420 nm. The rise time of the PMT is 0.78 ns. The wavelength region observed in the present experiment is centered at 382.5 nm and is 25 nm wide. This wavelength region covers the entire 0–0 band of the CN violet emission.

The optical axis of the spectrometer lies in a plane parallel to the end wall at 3.0 mm distance, as shown in Fig. 2. In the observed region, the flow is stationary and has undergone the shock-heating process twice, once by the primary shock and again by the immediately following reflected shock. The time between the arrivals of those two shocks is negligibly short, and so rare chemical reactions are expected. The process is effectively the same as a single strong shock wave that produces the same postshock enthalpy and pressure. The equivalent initial pressure was determined by the normal shock relations as the pressure to produce the measured postshock pressure for U_{eq}.

C. Calibration of the Spectrometer

The voltage signal produced by the PMT is converted into absolute intensity (W/cm^2-sr) by calibrating the spectrometer. In the calibration process, the spectrometer is moved out from the shock tube and placed in front of a light source with the external optical arrangement being kept unchanged. The same type of sapphire window as the test-section window is placed in front of the entrance slit of the spectrometer. A calibrated tungsten ribbon lamp is used as the radiance standard. It has a color temperature of 2373 K at 650 nm. Because the radiance data in wavelength range other than 650 nm are not given, we determined them using the CCD array detector. For this purpose, we used a DXW compact coil filament lamp calibrated as an irradiance standard by a NIST-certified group over the wavelength range from 250 to 1200 nm. The relative spectral response of the CCD array detector is determined by using this lamp. The absolute sensitivity of the system is determined by combining the absolute sensitivity at 650 nm and the relative sensitivity. The spectral radiance obtained in that manner is shown in Fig. 3, along with those of a black body at two different temperatures. One is the color temperature of the tungsten lamp (2373 K) and the other is the temperature corrected for the known emittance of tungsten (2913 K).

The radiance of the tungsten lamp is then measured by the PMT at the desired configuration of the spectrometer for the shock-tube measurement. A 50-kΩ resistor is used as the load resistor in the PMT circuit. The measurement is repeated five times and the average value is taken. The conversion factor for PMT voltage into the radiance (W/cm^2-sr) is then determined by comparing the measured voltage and the radiation intensity integrated over the wavelength range set by the exit slit opening, which is 25 nm.

D. Experimental Accuracy

It has been well known within the community that the main source of error in radiation measurement in a shock tube is the so-called

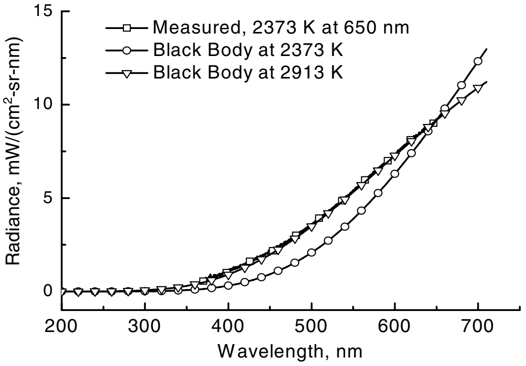

Fig. 3 Measured spectral radiance of the tungsten ribbon lamp.

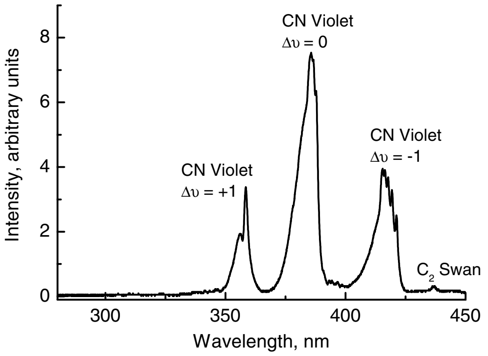

Fig. 4 Sample spectrum measured at $U_{eq} = 5.3$ km/s.

fatigue phenomenon of a PMT: the gain of a PMT decreases with time when it is receiving a light signal. The phenomenon is caused by accumulation of stray electrons in the tube when current is flowing. During calibration, a PMT is receiving signal over an extended length of time, whereas in a shock-tube test, signal lasts only for a short time. Fatigue occurs during calibration but not during a shock-tube run. For this reason, the fatigue characteristics of the PMT used was studied carefully. The input slit of the spectrometer is initially masked by a cover and then exposed by removing the cover. The measured signal showed that the exposure process was completed within 1.5 ms. After the transition, the signal was held at a constant level, which indicates that the fatigue phenomenon did not take place. Intensity values obtained in the calibration process were reproduced within 10% for all of the acquisitions.

This absence of fatigue phenomenon may be attributed to the extreme smallness of the PMT used. The PMT is packaged in a standard TO-8 casing that measures 16 mm in diameter and 11 mm in length. The inner volume of the PMT is several orders of magnitude smaller than the conventional PMTs. Possibly, the volume is instantly saturated with stray electrons.

Temporal resolution of the shock-tube measurement is estimated from the response time of the PMT circuit. Response time of the PMT circuit is less than 100 ns considering the rise time of the PMT itself and the load resistor of 50 Ω. Because the optical path is aligned using the optical alignment laser, the angular deviation of the external optics of the spectrometer from the plane of the shock front is expected to be less than 5 deg, which leads to a spatial resolution of less than 2 mm.

It has been reported by Byron [13] that the interaction of the reflected shock with the wall boundary layer causes shock bifurcation at the wall. This problem is addressed in the works of Appleton [14,15] and Burmeister [16], in which the reaction rate measurement was made in the reflected-shock region in the same manner as in the present work. They concluded that this effect is negligible in a rate measurement because measurement is usually finished before the boundary-layer effect becomes significant. In [14], measurements made with the reflecting end wall moved to within 3 mm of the edge of the windows gave the same measurement results as were obtained with the end wall moved to 10 mm. In that work, the shock speed was about 2.7 km/s and the initial pressure ranged from 0.5 to 2.0 torr, which is comparable with the present test conditions.

E. Measured Data

Figure 4 shows a time-integrated spectrum obtained at the equivalent shock velocity of 5.3 km/s. The three major vibrational manifolds of the CN violet system are observed. The intensity of the C_2 Swan band is very small. The spectral measurement confirmed that the emission intensity from other species, including the possible impurities of the shock tube, is negligibly low in the wavelength region of our interest.

Table 1 Test conditions for the temporal measurement

Case	U_s, km/s	U_{eq}, km/s	P_1, torr	P_{1eq}, torr	P_5, atm	T_5, K
1	3.45	5.20	1.3	3.77	1.36	12365
2	3.2	4.83	2.6	7.3	2.31	10650
3	3.4	5.13	2.6	8.37	2.99	12033

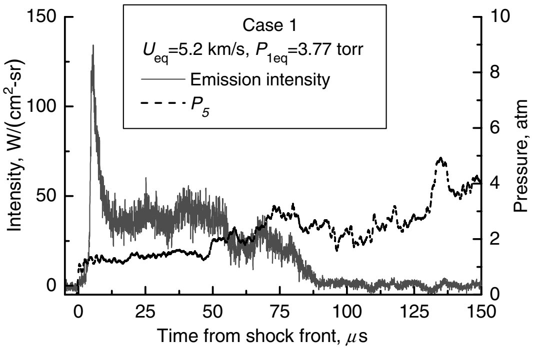

a) Case 1

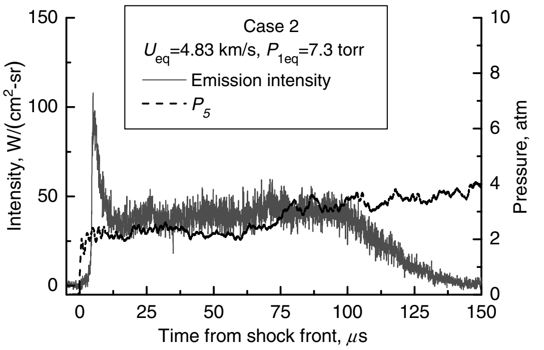

b) Case 2

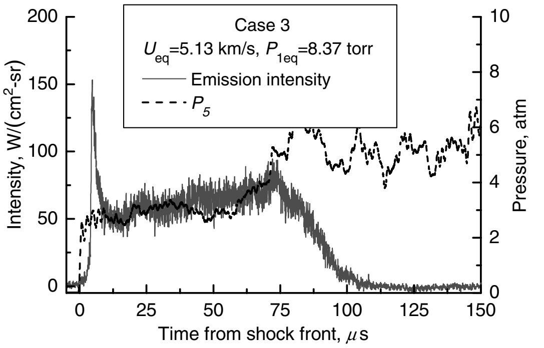

c) Case 3

Fig. 5 Measured intensity and pressure behind the reflected shock.

Temporal behavior of the CN emission is observed using the PMT for three different test conditions. The U_{eq} and P_{1eq} are calculated from the measured shock speed and end-wall pressure. The test conditions are listed in Table 1. The equilibrium temperature produced in case 1 is about 6100 K and it corresponds to that of Martian entry flight at 6.4 km/s.

Figures 5a–5c present the measured intensity and pressure profiles behind the reflected shock for the three test cases. A nonequilibrium peak is seen immediately behind the shock front in every test case. The peak relaxes into a plateau value with an abrupt decline following the plateau. That decline is consistently visible in all the test cases: at around 55 μs, 100 μs, and 75 μs for cases 1, 2, and 3, respectively. A distinct pressure jump accompanies the decline for cases 1 and 3. Those jumps are thought to be due to the disturbance of the flow by the arrival of the diaphragm debris and their vaporization. A weak emission is observed behind the primary shock region. This indicates that the gas is heated by the primary shock and CN is produced, however, the magnitude is small compared with the peak

Table 2 Comparison between the PL model and the PLGT model, shown in bold

	Reaction, $k_f = CT_x^n \exp(-T_d/T_x)$	M	T_x	C, cm^3 mole^{-1} s^{-1}	n	T_d	Source
	Dissociation						
1.	$C_2 + M \rightarrow C + C + M$	All	T_a	3.7×10^{14}	0.00	69,900	Park [2]
				$\mathbf{1.5 \times 10^{16}}$	**0.00**	**71,600**	**Gokcen** [20]
2.	$N_2 + M \rightarrow N + N + M$		T_a	7.0×10^{21}	−1.60	113,200	Park [2]
		C, O, N		3.0×10^{22}			Park [2]
		e$^-$		1.2×10^{25}			Park [2]
		e$^-$		$\mathbf{3.0 \times 10^{24}}$			**Gokcen** [20]
3.	$O_2 + M \rightarrow O + O + M$		T_a	2.0×10^{21}	−1.50	59,750	Park [2]
		C, O, N		1.0×10^{22}			Park [2]
4.	$CN + M \rightarrow C + N + M$	All	T_a	2.5×10^{14}	0.00	71,000	Park [2]
				$\mathbf{2.53 \times 10^{14}}$	**0.00**	**71,000**	**Gokcen** [20]
5.	$CO + M \rightarrow C + O + M$		T_a	2.3×10^{20}	−1.00	129,000	Park [2]
		C, O, N		3.4×10^{20}			Park [2]
6.	$NO + M \rightarrow N + O + M$		T_a	5.0×10^{15}	0.00	75,500	Park [2]
		C, O, N, NO, CO$_2$		1.1×10^{17}			Park [2]
		$\mathbf{N_2}$	$\boldsymbol{T_a}$	$\mathbf{1.45 \times 10^{15}}$	**0.00**	**74,700**	**Tsang** [21]
		$\mathbf{CO_2}$	$\boldsymbol{T_a}$	$\mathbf{2.41 \times 10^{15}}$	**0.00**	**74,700**	**Tsang** [21]
		The others	$\boldsymbol{T_a}$	$\mathbf{9.64 \times 10^{14}}$	**0.00**	**74,700**	**Tsang** [21]
7.	$CO_2 + M \rightarrow CO + O + M$		T_a	6.9×10^{21}	−1.50	63,275	Park [2]
		C, O, N		1.4×10^{22}			Park [2]
8.	$NCO + M \rightarrow CO + N + M$	All	T_a	6.3×10^{16}	−0.50	24,000	Park [2]
	Neutral exchange						
9.	$N_2 + O \rightarrow NO + N$		T	6.4×10^{17}	−1.00	38,370	Park [2]
10.	$NO + O \rightarrow O_2 + N$		T	8.4×10^{12}	0.00	19,450	Park [2]
11.	$CO + C \rightarrow C_2 + O$		T	2.0×10^{17}	−1.00	58,000	Park [2]
12.	$CO + O \rightarrow O_2 + C$		T	3.9×10^{13}	−0.18	69,200	Park [2]
13.	$CO + N \rightarrow CN + O$		T	1.0×10^{14}	0.00	38,600	Park [2]
14.	$N_2 + C \rightarrow CN + N$		T	1.1×10^{14}	−0.11	23,200	Park [2]
				$\mathbf{5.24 \times 10^{13}}$	**0.00**	**22,600**	**Gokcen** [20]
15.	$CN + O \rightarrow NO + C$		T	1.6×10^{13}	0.10	14,600	Park [2]
16.	$CN + C \rightarrow C_2 + N$		T	5.0×10^{13}	0.00	13,000	Park [2]
17.	$CO + CO \rightarrow C + CO_2$		T	2.3×10^{9}	0.50	65,710	Losev [19]
18.	$CO_2 + O \rightarrow O_2 + CO$		T	2.1×10^{13}	0.00	27,800	Park [2]
19.	$\mathbf{C_2 + N_2 \rightarrow CN + CN}$		$\boldsymbol{T}$	$\mathbf{1.5 \times 10^{13}}$	**0.00**	**21,000**	**Gokcen** [20]
20.	$CO + NO \rightarrow NCO + O$		T	3.8×10^{17}	−0.873	51,600	Park [2]
21.	$CN + O_2 \rightarrow NCO + O$		T	6.6×10^{12}	0.00	−200	Park [2]
22.	$CN + CO_2 \rightarrow NCO + CO$		T	4.0×10^{14}	0.00	19,200	Park [2]
23.	$CN + NO \rightarrow NCO + N$		T	1.0×10^{14}	0.00	21,200	Park [2]
24.	$CN + CO \rightarrow NCO + C$		T	1.5×10^{16}	−0.487	65,800	Park [2]
25.	$CO + N \rightarrow NO + C$		T	2.9×10^{11}	0.50	53,630	Losev [19]
26.	$NO + CO \rightarrow CO_2 + N$		T	4.6×10^{8}	0.50	12,070	Losev [19]
	Charge exchange						
27.	$NO^+ + C \rightarrow NO + C^+$		T	1.0×10^{13}	0.00	23,200	Park [2]
	Ionization						
28.	$O + N \rightarrow NO^+ + e^-$		T	8.8×10^{8}	1.00	31,900	Park [2]
29.	$C + e^- \rightarrow C^+ + e^- + e^-$		T_v	3.9×10^{33}	−3.78	130,700	Park [2]

value. The behavior of nonequilibrium radiation is assumed here to be independent of the process occurring before the nonequilibrium peak in the present work.

III. Numerical Simulations

Numerical simulations are performed using a computer code named Shock-Tube Mars (STMARS), which was developed in the

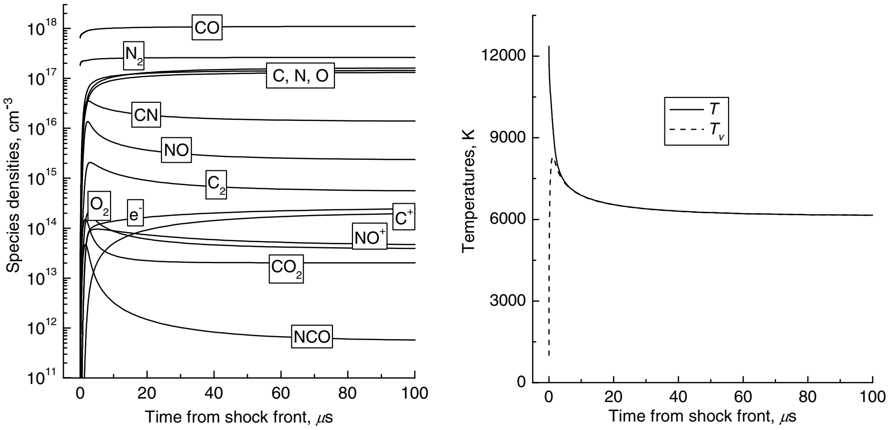

a) Species densities.

b) Translational-rotational and vibrational-electron-electronic temperatures.

Fig. 6 Calculation results of the PL model downstream of the shock for case 1.

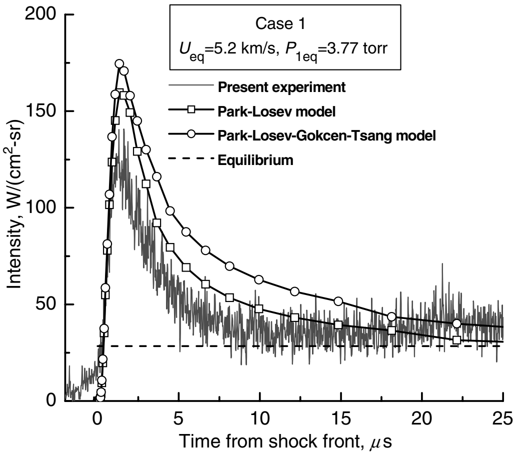

a) Case 1

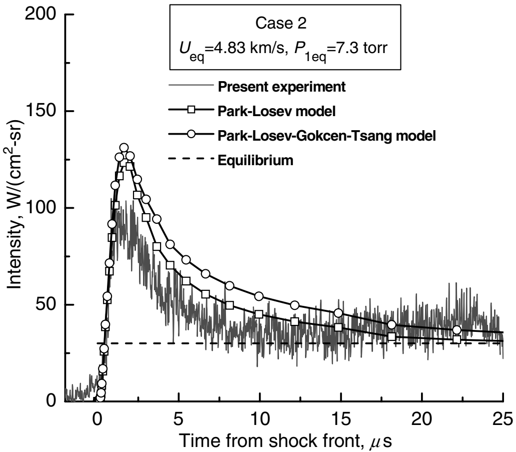

b) Case 2

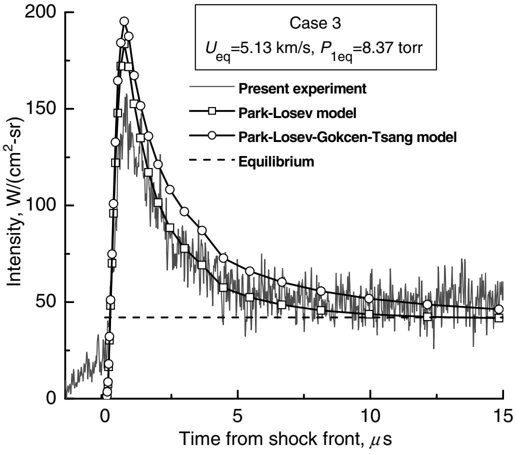

c) Case 3

Fig. 7 Comparison of the PL and PLGT results with measurements.

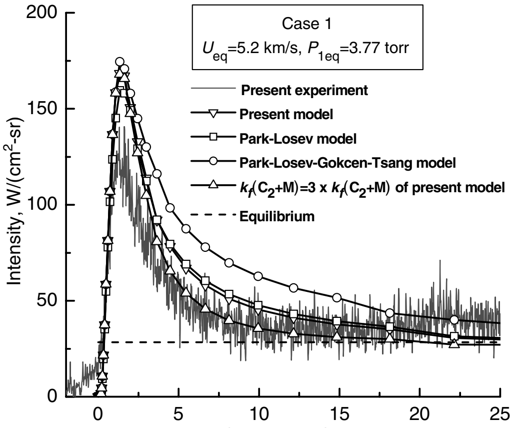

a) Case 1

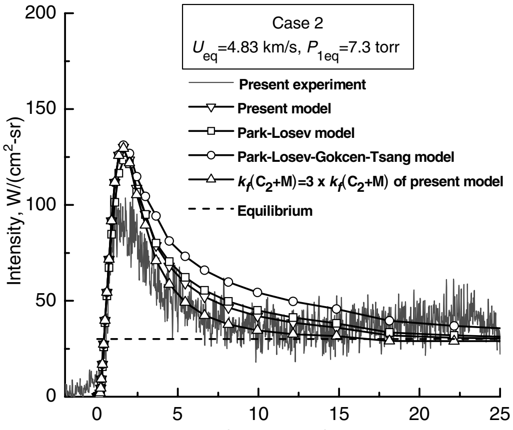

b) Case 2

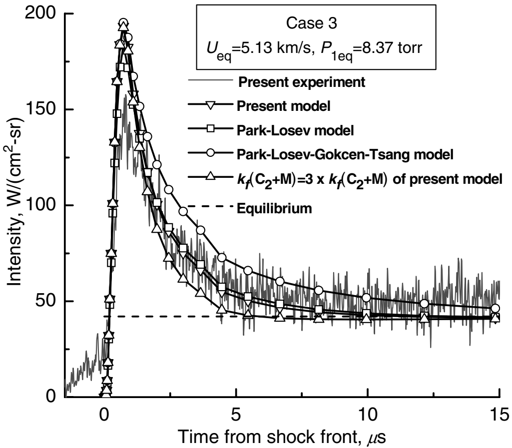

c) Case 3

Fig. 8 Comparison of the present model with the PL model, PLGT model, and measurements.

present work. In the STMARS code, the nonequilibrium reacting flow properties are computed for a one-dimensional flow in a constant-area duct. The two-temperature model by Park [17] is employed for the thermodynamic nonequilibrium in the code. Vibrational energy exchange is modeled using a Landau–Teller formulation with the relaxation times given by the Millikan and White expression [18]. Details of the thermal nonequilibrium modelings used in the STMARS code are described in [2]. The initial conditions are calculated by the normal shock relations using U_{eq} and P_{1eq}, assuming a thermochemically frozen flow and immediate equilibration between rotational and heavy-particle translational temperature.

Chemical species considered are C, O, N, CO, C_2, N_2, CN, NO, O_2, CO_2, C^+, NO^+, NCO, and e^-. Among the ionized species, only C^+ and NO^+ are considered here because the vibrational-electron-electronic temperature reaches, at most, about 8000 K under the present test conditions. Two different chemical rate schemes are first tested. For the first model, a set of 29 reactions is assembled from Park's [2] and Losev's [19] models. The rate coefficient values of the 26 reactions common in these two models are nearly the same. For these reactions, Park's values are used. For the reactions missing in Park's model, Losev's values are used. We hereafter refer to the merged version of these two models as the Park–Losev (PL) model.

Another chemical kinetic model is developed by modifying the PL model by using Gokcen's model [20] and Tsang's data [21]: One reaction, $C_2 + N_2 \rightarrow CN + CN$, is added and rate coefficients of five reactions are replaced by Gokcen's values. The rate coefficient of NO dissociation reaction is replaced by Tsang's data. The model developed here is referred to as the Park–Losev–Gokcen–Tsang (PLGT) model. The reactions and the corresponding rate coefficients of the PL and PLGT models are compared in Table 2.

Sample density and temperature profiles obtained by the PL model are presented in Fig. 6. The CN molecule is produced to a considerable concentration throughout the postshock region. Density of NCO is low in the equilibrium region (10^{-7}), whereas it overshoots to an amount comparable with O_2, NO^+, and e^- in the nonequilibrium region. The times taken for CO_2 and NCO to reach the peak are shorter than those of the other species by about 35%. Though not shown, it is observed that the increased initial pressure leads to fast relaxation of chemical compositions and temperatures.

The radiation along a given line of sight is computed in a subroutine named RADCAL, which is taken from [22]. In the subroutine, the spectral emission and absorption coefficients are obtained at the given thermochemical environment using a line-by-line technique. The transition probability values of the CN violet bands are taken from the work of Laux [23]. The internal states of the CN molecule are assumed to be populated according to the Boltzmann distribution defined by the vibrational-electron-electronic temperature. The well-known radiative transfer equation is integrated across the test section. The resulting intensity values are integrated over the 25-nm wavelength interval of observation.

IV. Comparison with Experiment

The calculation predicted the times taken for the reflected shock to travel from the end wall to the observation point to be about 4 μs. The time counts of the measurements are shifted backward based on this prediction. The experimental results are compared with the calculations using the two models in Figs. 7a–7c for the three cases. As seen in the figures, the intensity reaches a near-equilibrium value at the end of 15 μs for all three cases. Both models overpredict the intensity at the nonequilibrium peak for all cases. This discrepancy is believed to be due to the diffusive behavior of the peak radiation. Accepting this discrepancy in the peak-radiation value, we will judge the accuracy of a theoretical model by the decay rate of the CN radiation determined by the e-folding time of the decay curve.

As an alternative explanation to the low measured peak intensity, the assumption of Boltzmann distribution of internal states is examined. The population of the internal energy states does not follow the Boltzmann distribution in a nonequilibrium region, which results in a lowered nonequilibrium intensity [24]. However, [24] shows that the effect of the nonequilibrium population of the internal energy states diminishes as pressure increases: The nonequilibrium effect is significant when the postshock pressure is between 0.02 and 0.038 atm and is insignificant at 0.43 atm. The nonequilibrium effect is believed to be small in the present test conditions because the pressure behind the reflected shock ranges from 1.36 to 2.99 atm.

Table 3 Comparison between the PLGT model and present model, shown in bold

	Reaction, $k_f = CT_x^n \exp(-T_d/T_x)$	M	T_x	C, cm^3 mole^{-1} s^{-1}	n	T_d	Source
	Dissociation						
1.	$C_2 + M \rightarrow C + C + M$	All	T_a	1.5×10^{16}	0.00	71,600	Gokcen [20]
				7.5×10^{16}	**0.00**	**71,600**	**This work**
2.	$N_2 + M \rightarrow N + N + M$		T_a	7.0×10^{21}	−1.60	113,200	Park [2]
		C, O, N		3.0×10^{22}			Park [2]
		e^-		3.0×10^{24}			Gokcen [20]
3.	$O_2 + M \rightarrow O + O + M$		T_a	2.0×10^{21}	−1.50	59,750	Park [2]
		C, O, N		1.0×10^{22}			Park [2]
4.	$CN + M \rightarrow C + N + M$	All	T_a	2.53×10^{14}	0.00	71,000	Gokcen [20]
5.	$CO + M \rightarrow C + O + M$		T_a	2.3×10^{20}	−1.00	129,000	Park [2]
		C, O, N		3.4×10^{20}			Park [2]
6.	$NO + M \rightarrow N + O + M$		T_a	9.64×10^{14}	0.00	74,700	Tsang [21]
		N_2		1.45×10^{15}			Tsang [21]
		CO_2		2.41×10^{15}			Tsang [21]
7.	$CO_2 + M \rightarrow CO + O + M$		T_a	6.9×10^{21}	−1.50	63,275	Park [2]
		C, O, N		1.4×10^{22}			Park [2]
8.	$NCO + M \rightarrow CO + N + M$	All	T_a	6.3×10^{16}	−0.50	24,000	Park [2]
	Neutral exchange						
9.	$N_2 + O \rightarrow NO + N$		T	6.4×10^{17}	−1.00	38,370	Park [2]
10.	$NO + O \rightarrow O_2 + N$		T	8.4×10^{12}	0.00	19,450	Park [2]
11.	$CO + C \rightarrow C_2 + O$		T	2.0×10^{17}	−1.00	58,000	Park [2]
12.	$CO + O \rightarrow O_2 + C$		T	3.9×10^{13}	−0.18	69,200	Park [2]
13.	$CO + N \rightarrow CN + O$		T	1.0×10^{14}	0.00	38,600	Park [2]
14.	$N_2 + C \rightarrow CN + N$		T	5.24×10^{13}	0.00	22,600	Gokcen [20]
15.	$CN + O \rightarrow NO + C$		T	1.6×10^{13}	0.10	14,600	Park [2]
16.	$CN + C \rightarrow C_2 + N$		T	5.0×10^{13}	0.00	13,000	Park [2]
17.	$CO + CO \rightarrow C + CO_2$		T	2.3×10^{9}	0.50	65,710	Losev [19]
18.	$CO_2 + O \rightarrow O_2 + CO$		T	2.1×10^{13}	0.00	27,800	Park [2]
19.	$C_2 + N_2 \rightarrow CN + CN$		T	1.5×10^{13}	0.00	21,000	Gokcen [20]
20.	$CO + NO \rightarrow NCO + O$		T	3.8×10^{17}	−0.873	51,600	Park [2]
21.	$CN + O_2 \rightarrow NCO + O$		T	6.6×10^{12}	0.00	−200	Park [2]
22.	$CN + CO_2 \rightarrow NCO + CO$		T	4.0×10^{14}	0.00	19,200	Park [2]
23.	$CN + NO \rightarrow NCO + N$		T	1.0×10^{14}	0.00	21,200	Park [2]
24.	$CN + CO \rightarrow NCO + C$		T	1.5×10^{16}	−0.487	65,800	Park [2]
25.	$CO + N \rightarrow NO + C$		T	2.9×10^{11}	0.50	53,630	Losev [19]
26.	$NO + CO \rightarrow CO_2 + N$		T	4.6×10^{8}	0.50	12,070	Losev [19]
	Charge exchange						
27.	$NO^+ + C \rightarrow NO + C^+$		T	1.0×10^{13}	0.00	23,200	Park [2]
	Ionization						
28.	$O + N \rightarrow NO^+ + e^-$		T	8.8×10^{8}	1.00	31,900	Park [2]
29.	$C + e^- \rightarrow C^+ + e^- + e^-$		T_v	3.9×10^{33}	−3.78	130,700	Park [2]

In Figs. 7a–7c, the PLGT model consistently predicts slower decay rate compared with the PL model. The main difference between the PL and PLGT models is the rate coefficient of NO dissociation reaction. The rate coefficient in the PLGT model was determined from a shock-tube experiment, which is believed to be most reliable [21]. An effort is made here to improve the PLGT model to bring a better agreement between the measurement and calculation.

To find the reason for the slower decay rate in the PLGT model, we examined the rates of each reaction in the model. The dissociation reaction, $C_2 + M \rightarrow C + C + M$, was found to be most sensitive. Typically, the reaction rate changed by a factor of two for other reactions made insignificant difference to the emission intensity profile. The C_2 dissociation rate coefficient used in both PL and PLGT models was determined by shock-heating C_2H_2 in an argon bath (C_2H_2 composition no more than 500 ppm) [25]. The rate coefficient is invalid here because CO and N_2 are the major colliding partners. A C_2 dissociation rate coefficient increased five times is found to best reproduce the measured data. The factor of five is reasonable because most common gases are more efficient than argon as a third body. The third and the accepted set of reactions and corresponding rate coefficients determined in the present work is presented in Table 3 for the sake of completeness.

Figures 8a–8c compare the results of the present model with those of the PL and PLGT models. For comparison purposes, the case of the C_2 dissociation rate coefficient three times larger than the present value is shown. The present model produces the CN radiation decay rate closest to the experimental data. The PL model is close to the present model, but the PL model is not accepted here because the NO dissociation rate coefficient of the PL model is less reliable than that of the PLGT model. The three-times-larger C_2 dissociation rate seemingly produces absolute intensities closer to the experimental values, but its decay rate is faster.

V. Conclusions

In a CO–N_2 mixture heated to a temperature typical of Mars entry flight, the chemical reactions leading to the radiation of the CN violet system can best be described by a reaction scheme that combines the works of Park, Losev, Gokcen, and Tsang with the C_2 dissociation rate of Gokcen multiplied by a factor of five. It was experimentally confirmed that, after the nonequilibrium overshoot, the CN radiation approaches the predicted equilibrium value.

Acknowledgments

The authors express sincere thanks to Seong-Yoon Hyun and Youn-Gyu Jung of the Hypersonics and Biofluid Laboratory in the Department of Aerospace Engineering, who helped in conducting the shock-tube experiment.

References

[1] Lee, E. S., Chang, K. S., and Park, C., "Design Study of a Korean Mars Mission," *KSAS International Journal*, Vol. 5, No. 2, 2004, pp. 54–61.

[2] Park, C., Howe, J. T., Jaffe, R. L., and Candler, G. V., "Review of Chemical-Kinetic Problems of Future NASA Missions, 2: Mars Entries," *Journal of Thermophysics and Heat Transfer*, Vol. 8, No. 1, 1994, pp. 9–23.

[3] Seiff, A., and Kirk, D. B., "Structure of the Atmosphere of Mars in Summer at Mid-Latitudes," *Journal of Geophysical Research*, Vol. 82, No. 28, 1977, pp. 4364–4378.

[4] Arnold, J. O., Reis, V. H., and Woodward, H. T., "Theoretical and Experimental Studies of Equilibrium and Nonequilibrium Radiation to Bodies Entering Postulated Martian and Venusian Atmospheres at High Speeds," AIAA Paper 65-0166, Jan. 1965.

[5] Thomas, G. M., and Menard, W. A., "Experimental Measurements of Nonequilibrium and Equilibrium Radiation from Planetary Atmospheres," *AIAA Journal*, Vol. 4, No. 2, 1966, pp. 227–237.

[6] Nealy, J. E., and Haggard, K. V., "A Shock Tube Study of Radiation Behind Shock Waves in CO_2 with Application to Venus Entry," *Recent Developments in Shock Tube Research: Proceedings of the 9th International Symposium on Shock Tubes and Waves*, edited by D. Bershader, and W. Griffith, Stanford Univ. Press, Stanford, CA, 1973, pp. 330–339.

[7] Nealy, J. E., "An Experimental Study of Ultraviolet Radiation Behind Incident Normal Shock Waves in CO_2 at Venusian Entry Speeds," AIAA Paper 75-1150, Sept. 1975.

[8] Arnold, J. O., and Nicholls, R. W., "A Shock-Tube Determination of the CN Ground State Dissociation Energy and Electronic Transition Moments for the CN Violet and Red Band Systems," *Recent Developments in Shock Tube Research: Proceedings of the 9th International Symposium on Shock Tubes and Waves*, edited by D. Bershader, and W. Griffith, Stanford Univ. Press, Stanford, CA, 1973, pp. 340–351.

[9] Bogdanoff, D. W., and Park, C., "Radiative Interaction Between Driver and Driven Gases in an Arc-Driven Shock Tube," *Shock Waves*, Vol. 12, No. 3, 2002, pp. 205–214.

[10] Zalogin, G. N., Kozlov, P. V., Kuznetsova, L. A., Losev, S. A., Makarov, V. N., Romanenko, Yu. V., and Surzhikov, S. T., "Radiation Excited by Shock Waves in a CO_2-N_2-Ar Mixture: Experiment and Theory," *Technical Physics*, Vol. 46, No. 6, 2001, pp. 654–661.

[11] Losev, S. A., Kozlov, P. V., Kuznetsova, L. A., Makarov, V. N., Romanenko, Yu. V., Surzhikov, S. T., and Zalogin, G. N., "Radiation of a Mixture CO_2-N_2-Ar in Shock Waves: Experiment and Modeling," *Proceedings of the Third European Symposium on Aerothermodynamics for Space Vehicles*, ESTEC, Noordwijk, The Netherlands, Dec. 1998, pp. 437–444; also ESA Paper SP-426.

[12] Gorelov, V. A., Gladyshev, M. K., Kireev, A. Yu., Tchebureev, V. G., and Shilenkov, S. V., "Nonequilibrium Ionization and Radiation Behind Shock Wave in Martian Atmosphere," *Proceedings of the Third European Symposium on Aerothermodynamics for Space Vehicles*, ESTEC, Noordwijk, The Netherlands, Dec. 1998, pp. 429–436; also ESA Paper SP-426.

[13] Byron, S., "Shock-Tube Measurement of the Rate of Dissociation of Nitrogen," *Journal of Chemical Physics*, Vol. 44, No. 4, 1966, pp. 1378–1388.

[14] Appleton, J. P., and Steinberg, M., "Vacuum-Ultraviolet Absorption of Shock-Heated Vibrationally Excited Nitrogen," *Journal of Chemical Physics*, Vol. 46, No. 4, 1967, pp. 1521–1529.

[15] Appleton, J. P., Steinberg, M., and Liquornik, D. J., "Shock-Tube Study of Nitrogen Dissociation Using Vacuum-Ultraviolet Light Absorption," *Journal of Chemical Physics*, Vol. 48, No. 2, 1968, pp. 599–608.

[16] Burmeister, M., and Roth, P., "ARAS Measurements on the Thermal Decomposition of CO_2 Behind Shock Waves," *AIAA Journal*, Vol. 28, No. 3, 1990, pp. 402–405.

[17] Park, C., "Assessment of Two-Temperature Kinetic Model for Ionizing Air," *Journal of Thermophysics and Heat Transfer*, Vol. 3, No. 3, 1989, pp. 233–244.

[18] Millikan, R. C., and White, D. R., "Systematics of Vibrational Relaxation," *Journal of Chemical Physics*, Vol. 39, No. 12, 1963, pp. 3209–3213.

[19] Losev, S. A., and Chernyi, G. G., "Development of Thermal Protection System for Interplanetary Flight," International Science and Technology Center, Moscow State Univ., Rept. N 036-96, Moscow, Aug. 1999.

[20] Gokcen, T., "N_2-CH_4-Ar Chemical Kinetic Model for Simulations of Atmospheric Entry to Titan," AIAA Paper 2004-2469, June–Jul. 2004.

[21] Tsang, W., and Herron, J. T., "Chemical Kinetic Data Base for Propellant Combustion I. Reactions Involving NO, NO_2, HNO, HNO_2, HCN and N_2O," *Journal of Physical and Chemical Reference Data*, Vol. 20, No. 4, 1991, pp. 609–663.

[22] Whiting, E. E., Arnold, J. O., and Lyle, G. C., "A Computer Program for a Line-By-Line Calculation of Spectra from Diatomic Molecules and Atoms Assuming a Voigt Line Profile," NASA TN D-5088, Mar. 1969.

[23] Laux, C. O., "Optical Diagnostics and Radiative Emission of Air Plasmas," High Temperature Gasdynamics Laboratory, Stanford Univ., Rept. T-288, Stanford, CA, Aug. 1993.

[24] Bose, D., Wright, M. J., Bogdanoff, D. W., Raiche, G. A., and Allen, G. A., Jr., "Modeling and Experimental Assessment of CN Radiation Behind a Strong Shock Wave," *Journal of Thermophysics and Heat Transfer*, Vol. 20, No. 2, 2006, pp. 220–230.

[25] Kruse, T., and Roth, P., "Kinetics of C_2 Reactions During High-Temperature Pyrolysis of Acetylene," *Journal of Physical Chemistry A*, Vol. 101, No. 11, 1997, pp. 2138–2146.